Research Square

Preprints are preliminary reports that have not undergone peer review.
They should not be considered conclusive, used to inform clinical practice,
or referenced by the media as validated information.

Observation of light-induced Haldane gap in graphene

Shuyun Zhou

syzhou@mail.tsinghua.edu.cn

Tsinghua University https://orcid.org/0000-0002-9841-8610

Fei Wang

Tsinghua University

Xuanxi Cai

Tsinghua University https://orcid.org/0009-0004-6444-9541

Wanying Chen

Tsinghua University

Xiao Tang

Tsinghua University

Jinze Li

Tsinghua University https://orcid.org/0009-0007-0385-4801

Benshu Fan

Max Planck Institute for the Structure and Dynamics of Matter https://orcid.org/0000-0003-3845-5855

Tianshuang Sheng

Tsinghua University

Jinxi Lu

Tsinghua University

Jiansong Li

Tsinghua University

Hongyun Zhang

Tsinghua University https://orcid.org/0000-0002-0993-8949

Pu Yu

Tsinghua University https://orcid.org/0000-0002-5513-7632

Peizhe Tang

Beihang Univerisity https://orcid.org/0000-0002-6345-5809

Wenhui Duan

Tsinghua University https://orcid.org/0000-0001-9685-2547

Angel Rubio

Max Planck Institute for the Structure and Dynamics of Matter https://orcid.org/0000-0003-2060-3151

Zhiyuan Sun

Tsinghua University

Physical Sciences - Article

Keywords:

Posted Date: November 2nd, 2026

DOI: https://doi.org/10.21203/rs.3.rs-11148426/v1

License: This work is licensed under a Creative Commons Attribution 4.0 International License.
Read Full License

Additional Declarations: There is **NO** Competing Interest.

Observation of light-induced Haldane gap in graphene

Fei Wang[1,2,*], Xuanxi Cai[1,2,*], Wanying Chen[1,2,*], Xiao Tang[1,2], Jinze Li[1,2], Benshu Fan[3], Tianshuang Sheng[1,2], Jinxi Lu[1,2], Jiansong Li[1,2], Hongyun Zhang[1,2,4], Pu Yu[1,2,5], Peizhe Tang[3,6], Wenhui Duan[1,2,5], Angel Rubio[3,7,8], Zhiyuan Sun[1,2,5] & Shuyun Zhou[1,2,5,†]

[1]*Department of Physics, Tsinghua University, Beijing 100084, People's Republic of China*

[2]*State Key Laboratory of Low-Dimensional Quantum Physics, Tsinghua University, Beijing 100084, People's Republic of China*

[3]*Max Planck Institute for the Structure and Dynamics of Matter, Luruper Chaussee 149, 22761 Hamburg, Germany.*

[4]*Beijing Tsinghua Frontier Interdisciplinary Innovation Research Institute, Beijing, China*

[5]*Frontier Science Center for Quantum Information, Beijing 100084, People's Republic of China*

[6]*School of Materials Science and Engineering, Beihang University, Beijing 100191, People's Republic of China*

[7]*Initiative for Computational Catalysis and Center for Computational Quantum Physics, Simons Foundation Flatiron Institute, New York, New York 10010, USA*

[8]*Nano-Bio Spectroscopy Group and ETSF, Universidad del País Vasco UPV/EHU- 20018 San Sebastián, Spain*

** These authors contributed equally to this work*

† *Correspondence and request for materials should be sent to syzhou@mail.tsinghua.edu.cn*

Symmetry and topology, encoded in electronic wavefunctions, play a central role in the elec-

tronic properties and emergent phenomena of quantum materials. While these properties are conventionally determined by the equilibrium Hamiltonian, strong optical fields offer a fundamentally different route by reshaping the Hamiltonian on ultrafast timescales, turning symmetry and topology into dynamically controllable degrees of freedom. Graphene provides a paradigmatic platform for realizing this concept, where circularly polarized light has long been predicted to dynamically break time-reversal symmetry (TRS) and open a topologically nontrivial gap at the Dirac point. Despite extensive experimental efforts, direct observation of this Dirac gap—the defining spectroscopic signature of the dynamical TRS-breaking induced topological phase—has remained missing. Here we directly observe this light-induced Dirac gap in monolayer graphene. Time- and angle-resolved photoemission spectroscopy reveals that the gap emerges simultaneously with the optical field and exclusively under circularly polarized driving, directly linking its opening to dynamical TRS breaking. Together with Floquet theory, we identify the gap with a light-induced Haldane mass and reveal the associated nontrivial Floquet Berry curvature and Chern topology. By demonstrating dynamical TRS breaking in a prototypical non-magnetic material, our results establish optical driving as a route to ultrafast engineering of symmetry and topology, opening opportunities for dynamically tunable quantum matter beyond equilibrium.

Symmetry and topology are among the central concepts of the electronic structures and emergent phenomena of quantum materials[1–3]. Symmetries constrain the Hamiltonian and protect characteristic band degeneracies, while topology characterizes the global structure of electronic wavefunctions, giving rise to robust physical properties that are insensitive to microscopic details. In equilibrium, these properties are largely governed by crystal structure, magnetic order, static or quasistatic external fields. Of particular importance for electronic topology is time-reversal symmetry (TRS): breaking TRS removes the constraint on the net Berry curvature flux and enables nontrivial Chern topology, as exemplified by quantum Hall[4], quantum anomalous Hall[5,6] and fractional quantum anomalous Hall[7–10] systems.

Coherent light fields provide a new route to dynamically control TRS by engineering the electronic Hamiltonian on ultrafast timescales through strong light-matter coupling[11]. In the long-wavelength dipole approximation, the vector potential $\mathbf{A}(t)$ of the optical field enters the Bloch Hamiltonian as $H_0(\mathbf{k}) \rightarrow H_0[\mathbf{k} + e\mathbf{A}(t)/\hbar]$, where e is the elementary charge and $\hbar$ is the reduced Planck constant. By tuning the light polarization, frequency and amplitude, time-periodic driving provides a dynamical pathway to reshape the electronic band structures[12–14] with light-induced emergent phenomena[15–19]. Circularly polarized light is particularly intriguing because its handedness offers a route to dynamically break TRS even in a non-magnetic material (Fig. 1a). Under periodic driving, this symmetry breaking is encoded in an effective Hamiltonian[11] and has been predicted to endow the resulting Floquet states with nontrivial topology absent at equilibrium[20,21].

Graphene provides a paradigmatic system to test this possibility, whose massless Dirac

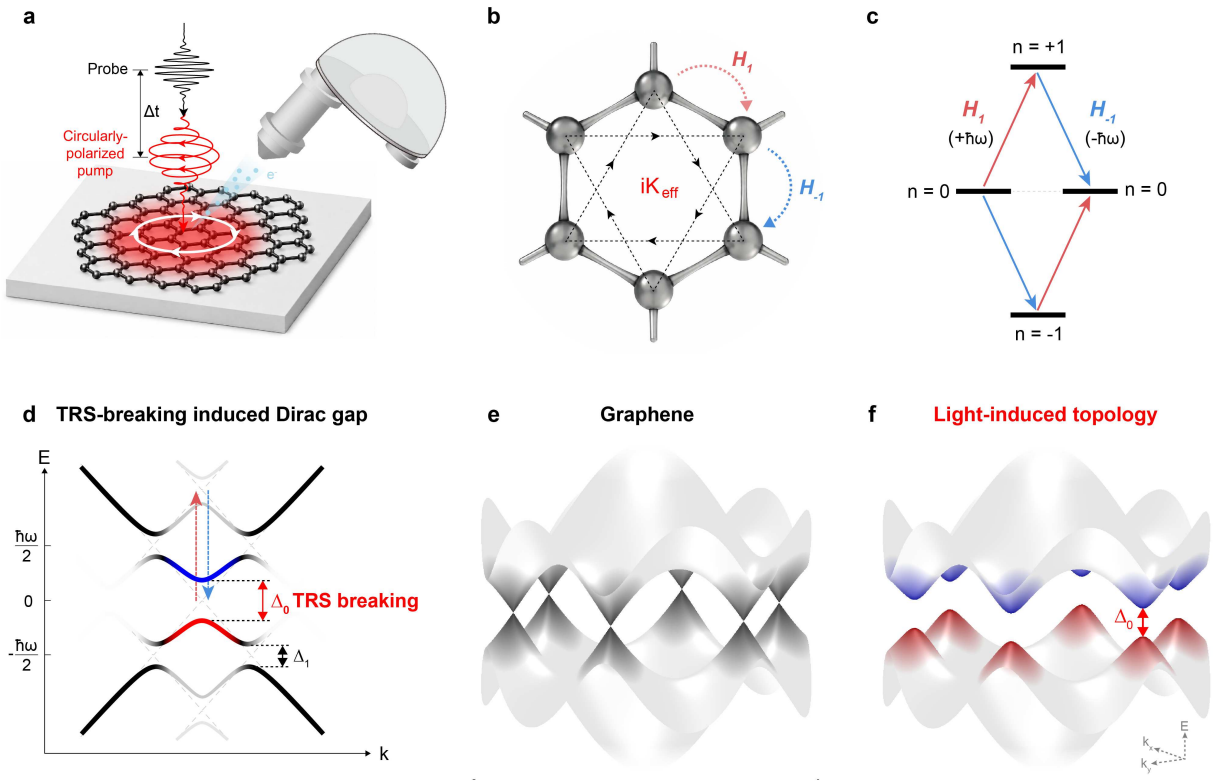


Fig. 1 | Schematic illustration of Floquet topological phases in irradiated graphene upon circularly polarized driving. **a**, Monolayer graphene under circularly polarized driving. **b**, The effective complex next-nearest-neighbor hopping iK_{eff} induced through virtual photon absorption-emission process. **c**, The Hamiltonian modification arises from a two-photon absorption-emission hopping process. **d**, Schematic electronic structure of irradiated graphene under circularly polarized driving. **e,f**, Schematic electronic structure of equilibrium graphene (**e**) and irradiated graphene under circularly polarized driving in the high frequency limit (**f**).

fermions are protected by inversion symmetry and TRS[22]. The Haldane model[2] demonstrated theoretically that TRS breaking can generate a topological gap and a Chern insulating state without a net magnetic flux. As a dynamical alternative to static TRS breaking, circularly polarized light was proposed to realize an analogous mechanism in graphene[11]. Second-order virtual photon absorption–emission processes, encoded by the $n = \pm 1$ Fourier components $H_{\pm 1}$ of the time-periodic Hamiltonian, generate an effective TRS-breaking mass term in the low-energy Floquet Hamiltonian[20,23], $\frac{[H_{-1},H_{+1}]}{\hbar\omega} = m_{\mathrm{F}}\sigma_z$, where m_{F} denotes the light-induced Floquet mass and σ_z is the Pauli matrix acting on the graphene sublattice pseudospin (Fig. 1b,c). It thus opens a Dirac gap and generates nonzero Floquet Berry curvature (Fig. 1d-f). This direct correspondence between symmetry breaking, Dirac-mass generation and topology makes graphene a canonical system for realizing light-induced topological state.

Experimental progress toward Floquet topological engineering in graphene has advanced from the detection of dressed Floquet states[24–28], to light-induced reconstruction of the electronic structure via the linearly polarized driving[29–31]. Crucially, the recent observation of avoided-crossing gaps at Floquet resonances established that experimentally accessible optical fields can directly reshape the electronic structure of graphene[29]. A central goal of Floquet topological engineering, however, is to move beyond electronic structure reconstruction and dynamically control the topology of electronic wavefunctions. In graphene, it is proposed that that circularly polarized light can achieve this by dynamically breaking TRS and opening a Haldane gap at the Dirac point[11,20,23,32]. Experimentally, light-induced anomalous Hall responses[33] and dichroic photocurrents[34] have provided important signatures consistent with this scenario. However, these

measurements probe the driven response rather than the topological electronic structure itself. Because such signals are strongly shaped by nonequilibrium carrier populations, scattering and dissipative dynamics[11,20,35–37], they cannot by themselves establish a TRS-breaking topological gap. The decisive missing evidence is a direct, energy- and momentum-resolved observation of the Dirac gap—the spectroscopic manifestation of light-induced Haldane mass. Such an observation would directly establish the emergence of non-trivial topology under circularly polarized driving, a long-standing goal of Floquet engineering in graphene.

Here by accessing the strong light–matter coupling regime, we directly observe this light-induced Dirac gap in monolayer graphene using time- and angle-resolved photoemission spectroscopy (TrARPES). The gap is observed exclusively under circularly polarized driving and emerges synchronously with the optical field, supporting its dynamical TRS-breaking origin, while theoretical calculations reveal the associated Floquet Berry curvature and Chern topology. Together, these results establish that an optical field can dynamically break TRS, thereby creating Floquet Chern state in a non-magnetic material.

Signature of Floquet-induced Dirac gap from the temporal evolution

Unambiguous identification of the light-induced Dirac gap Δ_0 requires an intrinsically gapless monolayer graphene. In epitaxial graphene, the substrate-induced equilibrium gap[38,39] and mid-gap states can obscure the genuine light-induced gap. We therefore use a large, highly uniform exfoliated monolayer graphene flake, enabling high-quality TrARPES data to reveal the sharp,

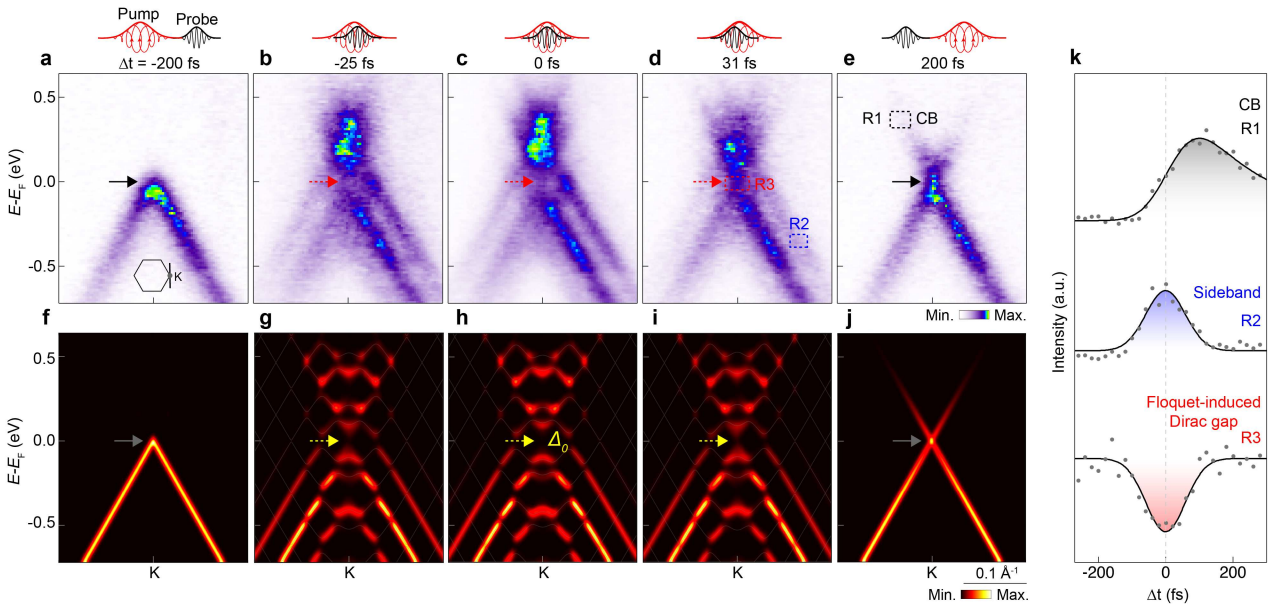


Fig. 2 | TrARPES signatures of light-induced electronic structure reconstruction in monolayer graphene. **a-e**, Dispersion images measured at different delay time Δt under circularly polarized driving with $\hbar\omega = 310$ meV at a pump fluence of 9.0 mJ/cm^2. The measurement direction is indicated by the black line in the inset. **f-j**, Simulated TrARPES spectra at different delay times. **k**, Integrated intensity of the photo-excited CB (1), sideband (2) and the Dirac point (3) as a function of delay time over regions marked in (d) and (e).

gapless Dirac cone (Extended Data Fig. 1). Resolving the topological Dirac gap further requires a qualitatively different driving regime from that used to observe first-order Floquet hybridization gaps[14,29,30]. Because the TRS-breaking gap arises from a higher-order Floquet effect[11], here we combine a low pump photon energy of $\hbar\omega = 310$ meV with typical fluence of 9.0 mJ/cm^2 (in-plane field strength 1.0×10^8 V/m on the sample) to enhance this interaction and bring the light-induced Dirac gap into an experimentally resolvable regime.

Figure 2 tracks the transient electronic structure across the pump–probe delay under circularly polarized driving. Before the pump pulse ($\Delta t = -200$ fs), graphene exhibits its equilibrium gapless Dirac dispersion with the Dirac point located at the Fermi level (Fig. 2a). When the pump overlaps with the probe (Fig. 2b-d), the electronic structure undergoes pronounced reconstruction, characterized by the Floquet sidebands separated by the pump photon energy and, more importantly, a strong suppression of spectral weight near the K point, providing the first indication of a transient Dirac gap. At 200 fs after the pump pulse, both features disappear and the Dirac cone dispersion is restored, while the upper Dirac cone remains transiently populated (Fig. 2e). Calculated spectra from Floquet theory reproduce these essential features, including the Floquet sidebands and the suppression of spectral weight near the Dirac point (Fig. 2f-j), supporting that they both arise from coherent coupling to the light field.

Because photo-excited carriers and coherent light-field dressing coexist during excitation, we distinguish their contributions through their distinct temporal dynamics. Figure 2k shows the evolution of the integrated intensities of the photo-excited conduction band (CB), the Floquet side-

band and the spectral weight near the Dirac point. Whereas the photo-excited CB population persists over several hundred femtoseconds before fully relaxing, both the Floquet sideband and the suppression of the spectral weight at the Dirac point are confined only to the pump–probe temporal-overlap region, distinguishing them from long-lived population effects. Their similar temporal evolution further identifies the intensity suppression near the Dirac point as a coherent Floquet response associated with the light-induced Dirac gap.

Extraction of light-induced Dirac gap under circularly polarized driving

Figure 3 directly resolves the light-induced Dirac gap by comparing the electronic structure at $\Delta t = 200$ fs and $\Delta t = 0$. At $\Delta t = 200$ fs, TrARPES resolves the intrinsic gapless Dirac cone (Fig. 3a). At temporal overlap under circularly polarized driving (Fig. 3b), a pronounced suppression of spectral weight near the K point is observed, accompanied by a clear separation of the upper and lower Dirac branches, providing direct spectroscopic evidence for gap opening at the Dirac point (Fig. 3b). Floquet calculations reproduce both the gap and the accompanying sidebands (Fig. 3c,d), supporting their light-induced origin.

The gap magnitude is further extracted from energy distribution curve (EDC) analysis (Fig. 3e-h). Whereas the EDC at $\Delta t = 200$ fs shows a single peak at the Dirac point, a clear splitting is observed at $\Delta t = 0$ (see the schematic comparison in Fig. 3i,j). Tracking the momentum-dependent peak positions allows us to extract the gapped dispersion (tick marks in Fig. 3f), where the separation of the upper and lower branches at the K point defines Δ_0. Fitting these peak positions gives

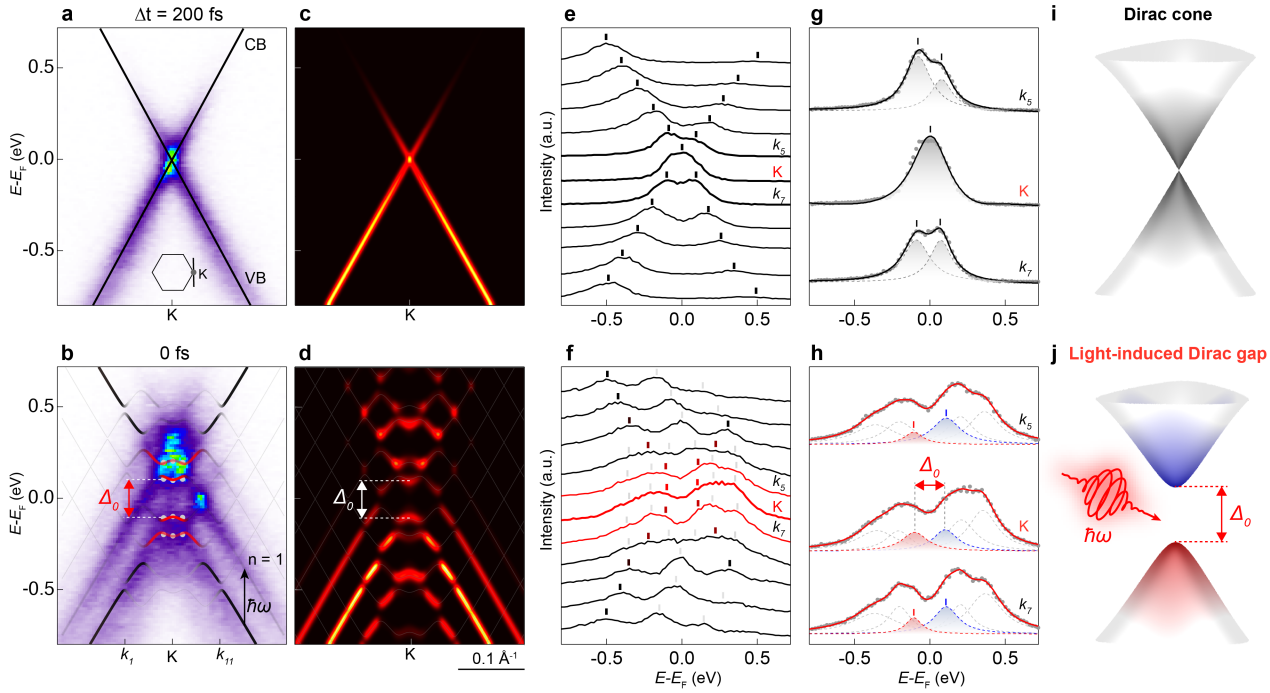


Fig. 3 | Experimental observation of Floquet-induced Dirac gap in monolayer graphene. a,b, Dispersion images measured at $\Delta t = 200$ fs (**a**) and $\Delta t = 0$ fs (**b**) under circularly polarized driving with $\hbar\omega = 310$ meV at a pump fluence of 9.0 mJ/cm^2. The calculated dispersions are over-plotted for comparison. **c,d**, Simulated TrARPES spectra at $\Delta t = 200$ fs (**c**) and $\Delta t = 0$ fs (**d**). **e,f**, EDCs extracted from (**a**) and (**b**) at the momentum positions marked in (**b**). The tick marks indicate the peak positions. **g,h**, EDCs at representative momentum positions (k_5, K and k_7) with fitting curves appended. **i,j**, Schematics of the gapless Dirac cone (**i**) and the Floquet-induced Dirac gap upon circularly polarized driving (**j**).

the gap value $\Delta_0 = 203 \pm 30$ meV (Fig. 3h). Furthermore, Δ_0 increases systematically with the pump fluence (Extended Data Fig. 2), consistent with the expected Floquet coupling dependence[40] and further supporting its Floquet-driven nature.

Polarization-selective dynamical TRS breaking

The dynamical TRS-breaking origin of the Dirac gap is established by its polarization dependence. Figure 4a-c compares the dispersion images measured at $\Delta t = 0$ under right- and left-circularly polarized (RCP and LCP) driving and linearly polarized (LP) driving with the light field parallel to the electron momentum. A pronounced Dirac gap opens under both RCP and LCP driving but is absent under LP excitation. Instead, LP driving results in only anisotropic avoided-crossings at Floquet resonances, consistent with previous observation in monolayer graphene[29]and graphite[30]. Floquet simulations in Fig. 4d-f reproduce this polarization selectivity, with a Dirac gap emerging exclusively under circular driving. Together, experimental and theoretical results identify the gap as a direct signature of dynamical TRS breaking.

The polarization dependence is further quantified by EDC analysis in Fig. 4g-j. Fitting the EDCs at the K point yields nearly identical gap magnitudes for RCP and LCP drivings (Fig. 4j), consistent with the Floquet TRS-breaking mechanism[11], where helicity reversal changes the sign of the induced Dirac mass while preserving its magnitude. Together, the exclusive emergence of the Dirac gap under circularly polarized driving and its helicity-independent magnitude distinguish the second-order TRS-breaking mass from first-order Floquet hybridization, establishing the observed

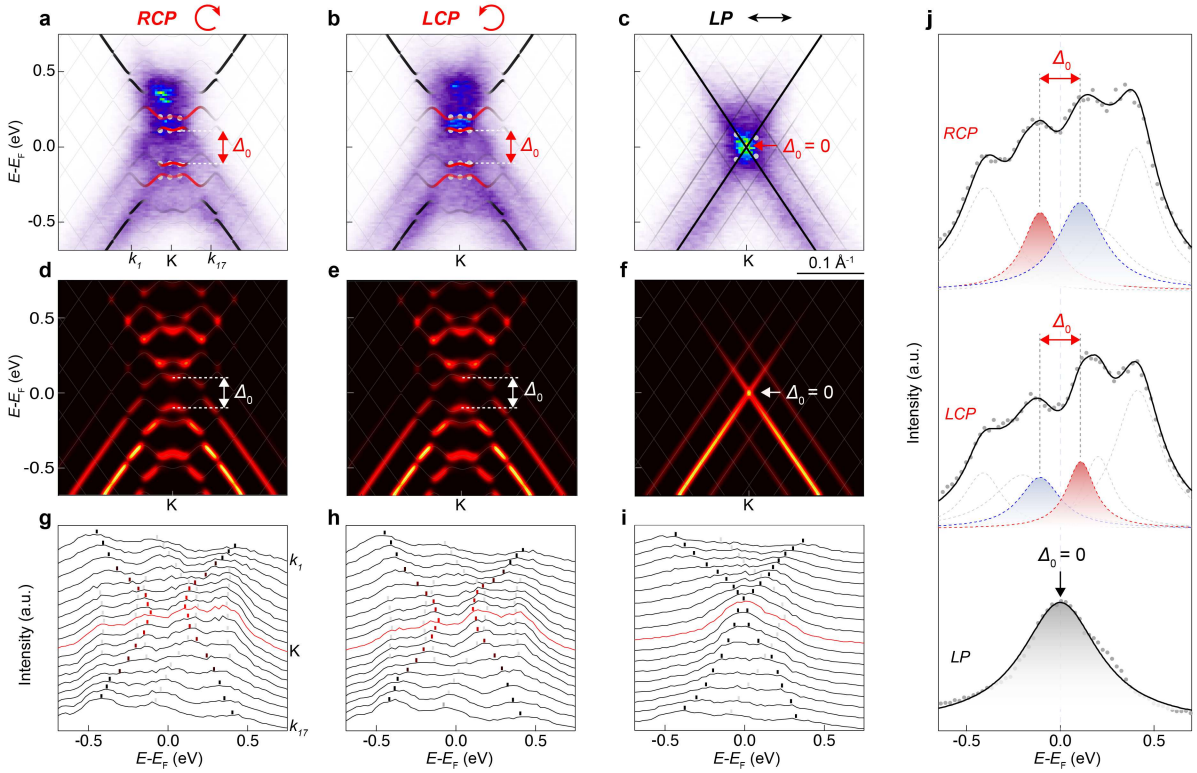


Fig. 4 | Floquet-induced TRS-breaking gap observed exclusively under circularly polarized driving. **a-c**, TrARPES dispersions measured under right- and left- circularly polarized driving (**a,b**) and linearly polarized driving (**c**). The pump photon energy is 310 meV and the pump fluence is 10 mJ/cm^2. The calculated dispersions are over-plotted for comparison. **d-f**, Corresponding simulations for different polarized driving. **g-i**, EDCs extracted from (**a-c**) at the momentum positions marked in (**a**). The tick marks indicate the peak positions. **j**, EDCs at the K point with fitting curves appended.

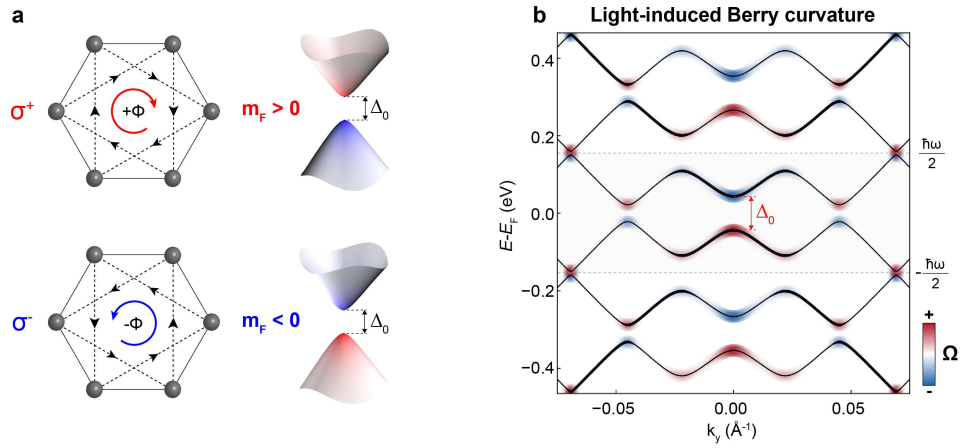


Fig. 5 | Light-induced Haldane mass and Berry curvature under circularly polarized driving. **a**, Schematic of RCP pump generating an effective chiral next-nearest-neighbor hopping, producing a Haldane mass, whose sign reverses for LCP pump. **b**, Theoretical Floquet electronic bands[11] with the Floquet Berry curvature encoded by the color scale.

gap as a direct spectroscopic signature of dynamical TRS breaking.

Light-induced Haldane mass and Floquet Berry curvature

The observation of the Dirac gap exclusively under circularly polarized driving provides direct evidence for a TRS-breaking Haldane mass underlying the Floquet topological bands in graphene[2, 11, 20]. In the high frequency expansion for the effective Hamiltonian, circularly polarized light generates Dirac masses of opposite sign at the K and K′ valleys, with both signs reversed upon reversing the light helicity (Fig. 5a). In real space, this mass arises from effective complex next-nearest-neighbor hoppings generated through second-order virtual photon processes (schematically illustrated in Fig. 1c), directly analogous to the Haldane model[2, 20]. This low-energy description applies

near the Dirac points for electronic energies well below the pump photon energy $\hbar\omega$. Combined with the opposite Dirac chiralities between the K and K′ valleys, the valley-opposite masses generate Floquet Berry curvatures of the same sign, providing the characteristic topological signature[20] analogous to the Haldane model (see Fig. 5 and Extended Data Fig. 3). Our measurements and calculations therefore establish a light-induced Haldane mass near the Dirac points and the associated low-energy Floquet Chern topology.

Discussion and perspectives

Our work establishes dynamical TRS breaking as a route to creating nontrivial electronic topology in a non-magnetic material. Previous realizations of light-induced TRS breaking have largely been limited to synthetic platforms[41,42] or to solids with pre-existing nontrivial topology or magnetic order[12,43,44]. Here, by contrast, optical driving generates a topological phase from an initially gapless, non-magnetic electronic system, driving graphene into a Chern state. More broadly, these results show that a fundamental symmetry conventionally determined by the equilibrium Hamiltonian can become a transient, optically tunable degree of freedom.

Dynamical TRS breaking provides a general route to optically transforming topological states, for example, driving Dirac or nodal-line semimetals into Weyl phases[45–49]. More fundamentally, it is not simply an optical analogue of a magnetic field: unlike static magnetic fields, it can break TRS without requiring magnetic order or spin polarization, providing access to symmetry-broken states beyond conventional magnetic approaches. This distinct route of symmetry control

may open access to chiral many-body states that are difficult to realize with static magnetic fields, for example, chiral spin liquids[50,51]. Moreover, combining light-induced Chern bands with strong electronic correlations may enable their fractionalization into Floquet fractional Chern insulating states[52], while related chiral interactions have been proposed to generate Floquet topological superconductivity[53]. Dynamical TRS breaking thus opens a new pathway for creating and controlling chiral quantum matter beyond equilibrium.

Methods

Sample preparation

High-quality monolayer graphene (MLG) samples were prepared using a clean dry-transfer method[54], following procedures similar to those developed for twisted bilayer graphene fabrication[55]. Briefly, MLG flakes were mechanically exfoliated onto a clean SiO_2/Si substrate. A graphite flake supported on a polydimethylsiloxane (PDMS) stamp was used to pick up the MLG under an optical microscope, forming a PDMS/graphite/MLG stack. After inverting the stack, the graphite/MLG heterostructure was retrieved using a second PDMS stamp and transferred onto Nb-doped TiO_2 or doped-Si substrates, leaving the MLG exposed at the top surface. A large twist angle between graphene and graphite was intentionally introduced to avoid forming moiré superlattice potential and preserve the intrinsic Dirac cone dispersion of MLG.

Prior to TrARPES measurements, the samples were annealed in the ultrahigh-vacuum chamber at 400°C until sharp electronic dispersions were obtained. All measurements were performed

at 80 K in an ultrahigh-vacuum chamber with a base pressure below 4×10^{-11} Torr.

Experimental setup

TrARPES measurements were performed using a home-built system at Tsinghua University. The laser source was a regenerative amplifier delivering 35 fs pulses centered at 800 nm (1.55 eV), with a pulse energy of 1.3 mJ and a repetition rate of 10 kHz. Probe pulses at 21.7 eV were generated by high-order harmonic generation (HHG) in argon driven by frequency-doubled 800 nm light and isolated using aluminium and tin filters[56]. The resulting probe pulses had a duration of 66 fs, providing sufficient temporal resolution to capture the Floquet-induced electronic reconstruction before electron-phonon and other relaxation processes become prominent[57]. The probe beam was focused onto the sample using a gold-coated toroidal mirror, producing a tightly-focused spot size of $57\,\mu\mathrm{m} \times 90\,\mu\mathrm{m}$ and enabling measurements of mechanically exfoliated graphene flakes.

Mid-infrared pump pulses with photon energy of 310 meV (wavelength of 4 μm) and pulse duration of 121 fs were generated by difference-frequency generation between the signal and idler outputs of an optical parametric amplifier[14]. Circularly polarized pump pulses were generated by passing through a quarter-wave plate designed for a center wavelength of 4 μm. The pump beam was incident nearly normal to the sample surface, at an angle of $0^\circ \pm 1^\circ$, ensuring a predominantly in-plane electric field. The degree of circular polarization was measured to be $95\% \pm 2\%$. The combination of high polarization purity and normal incidence geometry produces a highly circular, predominantly in-plane driving field, providing the conditions required for dynamical TRS breaking. In the TrARPES experiments, a typical pump fluence of 9.0 mJ/cm^2 was applied to

MLG, which corresponds to an electric field of $1.0 \pm 0.2 \times 10^8$ V/m at the sample after accounting for the Fresnel reflection, following the calculations in previous work[29].

Extraction of the Floquet-induced TRS-breaking gaps

To quantify the Floquet-induced Dirac gap at the K point, each EDC was obtained by integrating the spectral intensity over a momentum window of 0.014 Å^{-1}. Each EDC was fitted with six Lorentzian peaks to capture the two split Dirac-point peaks and their accompanying Floquet sideband peaks. The gap size, Δ_0, was defined as the energy separation between the two split peaks at the Dirac point. The uncertainty of the extracted gap was estimated as $\delta = \sqrt{\delta_{\mathrm{fit}}^2 + \delta_{\mathrm{sys}}^2}$, where δ_{fit} is the statistical fitting uncertainty and δ_{sys} is the systematic uncertainty evaluated by varying the momentum-integration window.

Calculation of the Floquet electronic structure

The Floquet electronic structures and time-resolved photoemission spectra were calculated using a tight-binding model of monolayer graphene. The equilibrium nearest-neighbour spinless Hamiltonian in the A/B sublattice basis is

$$H_0(\mathbf{p}) = -t_0 \begin{pmatrix} 0 & g(\mathbf{p}) \\ g^*(\mathbf{p}) & 0 \end{pmatrix}, \quad g(\mathbf{p}) = \sum_{j=1}^{3} e^{i\mathbf{p}\cdot\delta_j}\,, \tag{1}$$

where $\delta_1 = a_{\mathrm{C}}(0,1)$, $\delta_2 = a_{\mathrm{C}}(\sqrt{3}/2, -1/2)$ and $\delta_3 = a_{\mathrm{C}}(-\sqrt{3}/2, -1/2)$ are the three vectors connecting nearest-neighbor carbon atoms, $a_{\mathrm{C}} = 1.42$ Å is the C–C bond length, and the hopping amplitude is set to $t_0 = 3.09$ eV corresponding to the Dirac velocity $v_{\mathrm{F}} \simeq 1 \times 10^6$ m/s at the

K point. The pump field is introduced through minimal coupling, $H(\mathbf{p},t) = H_0(\mathbf{p} + e\mathbf{A}(t)/\hbar)$, where $\mathbf{A}(t) = A_0(\cos\omega t, \eta\sin\omega t)$ is the oscillating vector potential for circularly polarized light with the optical helicity $\eta = \pm 1$. The 'Hamiltonian' in Floquet space is $(H_{\rm F})_{mn} = H_{m-n} + m\hbar\omega\,\delta_{mn}\mathbb{I}$ where $H_\ell = \frac{1}{T}\int_0^T dt\, e^{-i\ell\omega t}H(t)$, m, n label the Floquet sectors and $T = 2\pi/\omega$. The electronic Floquet bands in Figs. 2-5 are obtained by diagonalizing $(H_{\rm F})_{mn}$. Convergence in the truncation $m, n = -N, \ldots, N$ is achieved with $N = 8$. In the next section, we discuss analytical understanding of the Floquet electronic structure.

Floquet Haldane mass and Berry curvature of the low energy electrons

The Haldane mass and Berry curvature are most conveniently understood from the standard high frequency expansion for the effective Floquet Hamiltonian[20], which works for electrons close to the K points and at energies much lower than the pump frequency ω. Close to the K points, the equilibrium Hamiltonian for the low energy Dirac electrons is $H_{0,\tau}(\mathbf{k}) = \hbar v_{\rm F}\left(\tau k_x\sigma_x + k_y\sigma_y\right)$, where the Pauli matrices σ_i act in the sublattice space and $\tau = +1$ (-1) corresponds to K (K′) valley. Under circularly polarized pump light with helicity $\eta = \pm 1$, to the lowest non-trivial order in $1/\omega$, virtual photon absorption and emission give the effective Floquet Hamiltonian[20]

$$H_{{\rm eff},\tau}(\mathbf{k}) \approx H_{0,\tau} + \frac{[H_{-1}, H_{+1}]}{\hbar\omega} = \hbar v_{\rm F}\left(\tau k_x\sigma_x + k_y\sigma_y\right) + \tau\eta m_{\rm F}\sigma_z \tag{2}$$

where $m_{\rm F} = \beta^2\hbar\omega$ and $\beta = ev_F A_0/(\hbar\omega) = ev_F E_0/(\hbar\omega^2)$. The Dirac gap is $\Delta_0 = 2|m_{\rm F}|$. From Eq. (2), the Haldane mass $m_\tau = \tau\eta m_{\rm F}$ has opposite signs at K and K′, while reversing the optical helicity reverses the signs of both. The Berry curvature of the conduction/valence band of $H_{{\rm eff},\tau}$ takes the analytical form $\Omega_{s,\tau}(\mathbf{k}) = -s\eta\,\frac{m_{\rm F}\hbar^2 v_{\rm F}^2}{2\left(\hbar^2 v_{\rm F}^2 k^2 + m_{\rm F}^2\right)^{3/2}}$, where $s = +1$ (-1) denotes the

conduction (valence) band. Between the two valleys, the opposite Dirac chiralities and opposite masses compensate, resulting in Berry curvatures of the same sign. It concentrates within the region of the characteristic momentum scale $k_{\mathrm{m}} = m_{\mathrm{F}}/(\hbar v_{\mathrm{F}})$. One may define the "partial Chern number" $C_\Lambda = \frac{1}{2\pi}\int_{|\mathbf{k}|<\Lambda} d^2k\,\Omega(\mathbf{k})$ by integrating the time-averaged Berry curvature over a circular momentum region with the cutoff Λ around the K point. For the valence band, one has $C_\Lambda = \eta\left(1-\frac{1}{\sqrt{1+(\Lambda/k_{\mathrm{m}})^2}}\right) \xrightarrow{\Lambda\gg k_{\mathrm{m}}} \eta$ where we have summed two valleys. We note again that this model works only for low electrons close to the K points, while the exact topological characterization of the Floquet band is discussed in the next section.

Exact Floquet Berry curvature and Floquet topology

The exact topological classification of the Floquet bands requires a shift from the equilibrium framework. Strictly speaking, the Floquet Berry curvature of a Floquet band α with the Floquet eigenstates $|\phi_{\alpha,\mathbf{k}}(t)\rangle$ is $\Omega_\alpha(\mathbf{k},t) = -i\nabla_{\mathbf{k}}\times\langle\phi_{\alpha,\mathbf{k}}(t)|\nabla_{\mathbf{k}}|\phi_{\alpha,\mathbf{k}}(t)\rangle$, which can vary with time within each driving cycle[21,58]. However, its integral over the full Brillouin zone, the Floquet Chern number $C_\alpha = \frac{1}{2\pi}\int_{\mathrm{BZ}} d^2\mathbf{k}\Omega_\alpha(\mathbf{k},t)$, is a topological invariant that is time-independent because smooth unitary evolution preserves the band topology[17,21,58–60]. Writing the Floquet eigen state wave function as $\phi_{\alpha,\mathbf{k}}(t) = e^{-i\varepsilon_\alpha t}\sum_n u_{\alpha n,\mathbf{k}}e^{-in\omega t}$ where n is the harmonic index, the time-averaged Berry curvature is calculated as $\Omega_\alpha(\mathbf{k}) = -2\,\mathrm{Im}\sum_n\langle\partial_{k_x}u_{\alpha n}|\partial_{k_y}u_{\alpha n}\rangle$. The corresponding partial Chern number C_Λ develops a plateau approaching $+1$ (-1) for RCP (LCP) for a substantial range of Λ (see Extended Data Fig. 3), indicating the Chern topology associated with the light-induced Haldane mass.

We now discuss the implications of such Floquet Chern topology. An integer Chern number does not imply a quantized Hall conductance as the Floquet bands are generally only partially occupied[11,20,35–37]. Its topological significance lies instead in the chirality of Floquet edge states. The net chirality of edge states crossing the quasienergy ε within a quasienergy gap is characterized by another topological invariant, the winding number W_ε[58] that is related to the Chern number. Note that these topological invariants are rigorously defined only globally over the whole Brillouin zone and are therefore sensitive to the weak higher-order resonances[61]. The experimentally relevant low-energy topology, however, remains clear: the observed Dirac gap is identified with a dynamically generated Haldane mass near the Dirac point, together with the associated Berry-curvature structure and low-energy chiral edge states[17,20].

Simulation of the time-resolved photoemission signal

In this section, we discuss the numerical calculation of the TrARPES intensity:

$$I_{\mathbf{k}}(\omega, \Delta t) = \sum_{ab} M_{a,\mathbf{k}} M^*_{b,\mathbf{k}} \int dt\, dt'\, s(t) s(t') e^{i\omega(t-t')} \mathcal{V}_{\mathbf{p}}(t,t') \left[-iG^<_{ab,\mathbf{k}}(t,t')\right]. \tag{3}$$

Here $a, b = A, B$ are the sublattice indices, $M_{a/b,\mathbf{k}}$ is the photoemission matrix element between the free space electronic state $\mathbf{p}$ and the Bloch state at crystal momentum $\mathbf{k}$ (equal to the in-plane momentum $\mathbf{p}_\parallel$ of the free space state in our experiment) formed from an a- or b-sublattice orbital, and $s(t)$ denotes the probe-pulse envelope which has a delay Δt relative to the pump. The lesser Green function is

$$G^<_{ab,\mathbf{k}}(t,t') = iU_{\mathbf{k}}(t,t_0)\rho_{0,ab,\mathbf{k}}U^\dagger_{\mathbf{k}}(t',t_0), \quad U_{\mathbf{k}}(t,t') = \mathcal{T}\exp\left[-(i/\hbar)\int_{t'}^{t} d\tau\, H(\mathbf{k},\tau)\right] \tag{4}$$

where $\rho_{0,ab,\mathbf{k}} = \langle c^\dagger_{a,\mathbf{k}} c_{b,\mathbf{k}} \rangle_0$ is the single particle density matrix determined by the equilibrium Fermi–Dirac distribution before the pump, $H(\mathbf{k}, \tau)$ is the time dependent single particle Hamiltonian including the pump field, and $\mathcal{T}$ denotes time ordering. For the TrARPES spectra shown in the main text, the simulations use an in-plane pump electric-field of $E_0 = 1.0 \times 10^8$ V/m at $\hbar\omega = 310$ meV. Crystal symmetry near the probed K point constrains the photoemission matrix elements for the near-normal-incidence probe. With the crystalline x axis along Γ–K, x- and y-polarized probes give $M_{A,\mathbf{k}} = M_{B,\mathbf{k}}$ and $M_{A,\mathbf{k}} = -M_{B,\mathbf{k}}$ at the K-point, respectively. Via the dynamical phase $\mathcal{V}_{\mathbf{p}}(t, t') = \exp\left[\frac{i}{\hbar}\int_{t'}^{t} d\bar{t}\, \delta\epsilon_V(\mathbf{p}_\parallel, \bar{t})\right]$, final-state Volkov dressing[26] is included where $\delta\epsilon_V(\mathbf{p}, t) = \frac{\hbar\mathbf{p}_\parallel}{m} \cdot e\mathbf{A}_V(t) + \frac{e^2 A_V^2(t)}{2m}$ is the pump-induced energy shift of the free space photoelectron. Here $\mathbf{p}_\parallel = \mathbf{k} + \mathbf{G}$ is its in-plane momentum, $\mathbf{k}$ is the crystal momentum of the initial state and $\mathbf{G}$ is a reciprocal-lattice vector. The vector potential acting on the free space photoelectron is $\mathbf{A}_V(t) = \alpha_V \mathbf{A}_{\mathrm{pump}}(t)$ where $\alpha_V = 0.7$ is a phenomenological coefficient. Note that this effect only dresses the free space photoelectron and leads to Floquet–Volkov interference, while it does not affect the Floquet bands of the Bloch electrons.

References

1. Thouless, D. J., Kohmoto, M., Nightingale, M. P. & den Nijs, M. Quantized Hall conductance in a two-dimensional periodic potential. Phys. Rev. Lett. **49**, 405 (1982).

2. Haldane, F. D. M. Model for a quantum Hall effect without Landau levels: condensed-matter realization of the "parity anomaly". Phys. Rev. Lett. **61**, 2015 (1988).

3. Kane, C. L. & Mele, E. J. Quantum spin Hall effect in graphene. Phys. Rev. Lett. **95**, 226801 (2005).

4. Klitzing, K. V., Dorda, G. & Pepper, M. New method for high-accuracy determination of the fine-structure constant based on quantized Hall resistance. Phys. Rev. Lett. **45**, 494 (1980).

5. Chang, C.-Z. et al. Experimental observation of the quantum anomalous Hall effect in a magnetic topological insulator. Science **340**, 167 (2013).

6. Deng, Y. et al. Quantum anomalous Hall effect in intrinsic magnetic topological insulator $MnBi_2Te_4$. Science **367**, 895 (2020).

7. Park, H. et al. Observation of fractionally quantized anomalous Hall effect. Nature **622**, 74 (2023).

8. Zeng, Y. et al. Thermodynamic evidence of fractional Chern insulator in moiré $MoTe_2$. Nature **622**, 69 (2023).

9. Xu, F. et al. Observation of integer and fractional quantum anomalous Hall effects in twisted bilayer $MoTe_2$. Phys. Rev. X **13**, 031037 (2023).

10. Lu, Z. et al. Fractional quantum anomalous Hall effect in multilayer graphene. Nature **626**, 759 (2024).

11. Oka, T. & Aoki, H. Photovoltaic Hall effect in graphene. Phys. Rev. B **79**, 081406 (2009).

12. Wang, Y., Steinberg, H., Jarillo-Herrero, P. & Gedik, N. Observation of Floquet-Bloch states on the surface of a topological insulator. Science **342**, 453 (2013).

13. Ito, S. et al. Build-up and dephasing of Floquet–Bloch bands on subcycle timescales. Nature **616**, 696 (2023).

14. Zhou, S. et al. Pseudospin-selective Floquet band engineering in black phosphorus. Nature **614**, 75 (2023).

15. Basov, D. N., Averitt, R. D. & Hsieh, D. Towards properties on demand in quantum materials. Nat. Mater. **16**, 1077 (2017).

16. Oka, T. & Kitamura, S. Floquet engineering of quantum materials. Annu. Rev. Condens. Matter Phys. **10**, 387 (2019).

17. Rudner, M. S. & Lindner, N. H. Band structure engineering and non-equilibrium dynamics in Floquet topological insulators. Nat. Rev. Phys. **2**, 229 (2020).

18. de la Torre, A. et al. Colloquium: nonthermal pathways to ultrafast control in quantum materials. Rev. Mod. Phys. **93**, 041002 (2021).

19. Bao, C., Tang, P., Sun, D. & Zhou, S. Light-induced emergent phenomena in 2D materials and topological materials. Nat. Rev. Phys. **4**, 33 (2022).

20. Kitagawa, T., Oka, T., Brataas, A., Fu, L. & Demler, E. Transport properties of nonequilibrium systems under the application of light: photoinduced quantum Hall insulators without Landau levels. Phys. Rev. B **84**, 235108 (2011).

21. Lindner, N. H., Refael, G. & Galitski, V. Floquet topological insulator in semiconductor quantum wells. Nat. Phys. **7**, 490 (2011).

22. Castro Neto, A. H., Guinea, F., Peres, N. M. R., Novoselov, K. S. & Geim, A. K. The electronic properties of graphene. Rev. Mod. Phys. **81**, 109 (2009).

23. Sentef, M. et al. Theory of Floquet band formation and local pseudospin textures in pump-probe photoemission of graphene. Nat. Commun. **6**, 7047 (2015).

24. Aeschlimann, S. et al. Survival of Floquet–Bloch states in the presence of scattering. Nano Lett. **21**, 5028 (2021).

25. Park, S. et al. Steady Floquet–Andreev states in graphene Josephson junctions. Nature **603**, 421 (2022).

26. Merboldt, M. et al. Observation of Floquet states in graphene. Nat. Phys. **21**, 1093 (2025).

27. Choi, D. et al. Observation of Floquet–Bloch states in monolayer graphene. Nat. Phys. **21**, 1100 (2025).

28. Madéo, J. & Dani, K. M. Floquet states in graphene revealed at last. Nat. Phys. **21**, 1040 (2025).

29. Wang, F. et al. Observation of Floquet-induced gap in graphene. Nat. Mater. **25**, 1140 (2026).

30. Wang, F. et al. Robust Floquet-induced gap in irradiated graphite. Chin. Phys. Lett. **43**, 050705 (2026).

31. Sentef, M. A. & Reutzel, M. A Floquet gap finally opens in graphene. Nat. Mater. **25**, 1080 (2026).

32. Liu, H., Troisi, F., Hübener, H., Latini, S. & Rubio, A. Cavity-mediated electron-electron interactions: Renormalizing Dirac states in graphene. Sci. Adv. **11**, eadz1855 (2025).

33. McIver, J. W. et al. Light-induced anomalous Hall effect in graphene. Nat. Phys. **16**, 38 (2020).

34. Lesko, D. M. B. et al. Optical control of electrons in a Floquet topological insulator. Nat. Phys. (2026). https://doi.org/10.1038/s41567-026-03429-7.

35. Sato, S. A. et al. Light-induced anomalous Hall effect in massless Dirac fermion systems and topological insulators with dissipation. New J. Phys. **21**, 093005 (2019).

36. Sato, S. A. et al. Microscopic theory for the light-induced anomalous Hall effect in graphene. Phys. Rev. B **99**, 214302 (2019).

37. Nuske, M. et al. Floquet dynamics in light-driven solids. Phys. Rev. Res. **2**, 043408 (2020).

38. Zhou, S. Y. et al. Substrate-induced bandgap opening in epitaxial graphene. Nat. Mater. **6**, 770 (2007).

39. Kim, S., Ihm, J., Choi, H. J. & Son, Y.-W. Origin of anomalous electronic structure of epitaxial graphene on silicon carbide. Phys. Rev. Lett. **100**, 176802 (2008).

40. Atteia, J., Bardarson, J. H. & Cayssol, J. Ballistic transport through irradiated graphene. Phys. Rev. B **96**, 245404 (2017).

41. Jotzu, G. et al. Experimental realization of the topological Haldane model with ultracold fermions. Nature **515**, 237 (2014).

42. Rechtsman, M. C. et al. Photonic Floquet topological insulators. Nature **496**, 196 (2013).

43. Bielinski, N. et al. Floquet–Bloch manipulation of the Dirac gap in a topological antiferromagnet. Nat. Phys. **21**, 458 (2025).

44. Chassot, F. et al. Floquet topological state induced by light-driven band inversion in SnTe. Nat. Phys. **22**, 1282 (2026).

45. Chan, C.-K., Oh, Y.-T., Han, J. H. & Lee, P. A. Type-II Weyl cone transitions in driven semimetals. Phys. Rev. B **94**, 121106(R) (2016).

46. Yan, Z. & Wang, Z. Tunable Weyl points in periodically driven nodal line semimetals. Phys. Rev. Lett. **117**, 087402 (2016).

47. Taguchi, K., Xu, D.-H., Yamakage, A. & Law, K. T. Photovoltaic anomalous Hall effect in line-node semimetals. Phys. Rev. B **94**, 155206 (2016).

48. Hübener, H., Sentef, M. A., De Giovannini, U., Kemper, A. F. & Rubio, A. Creating stable Floquet-Weyl semimetals by laser-driving of 3D Dirac materials. Nat. Commun. **8**, 13940 (2017).

49. Murotani, Y. et al. Disentangling the competing mechanisms of light-induced anomalous Hall conductivity in three-dimensional Dirac semimetal. Phys. Rev. Lett. **131**, 096901 (2023).

50. Claassen, M., Jiang, H.-C., Moritz, B. & Devereaux, T. P. Dynamical time-reversal symmetry breaking and photo-induced chiral spin liquids in frustrated Mott insulators. Nat. Commun. **8**, 1192 (2017).

51. Kitamura, S., Oka, T. & Aoki, H. Probing and controlling spin chirality in Mott insulators by circularly polarized laser. Phys. Rev. B **96**, 014406 (2017).

52. Grushin, A. G., Gómez-León, Á. & Neupert, T. Floquet fractional Chern insulators. Phys. Rev. Lett. **112**, 156801 (2014).

53. Kitamura, S. & Aoki, H. Floquet topological superconductivity induced by chiral many-body interaction. Commun. Phys. **5**, 174 (2022).

54. Wang, L. et al. One-dimensional electrical contact to a two-dimensional material. Science **342**, 614 (2013).

55. Li, Q. et al. Evolution of the flat band and the role of lattice relaxations in twisted bilayer graphene. Nat. Mater. **23**, 1070 (2024).

56. Zhong, H. et al. High harmonic generation light source with polarization selectivity and sub-100-μm beam size for time- and angle-resolved photoemission spectroscopy. Ultrafast Sci. **4**, 0063 (2024).

57. Gierz, I. et al. Snapshots of non-equilibrium Dirac carrier distributions in graphene. Nat. Mater. **12**, 1119 (2013).

58. Rudner, M. S., Lindner, N. H., Berg, E. & Levin, M. Anomalous edge states and the bulk-edge correspondence for periodically driven two-dimensional systems. Phys. Rev. X **3**, 031005 (2013).

59. Schüler, M. et al. How circular dichroism in time- and angle-resolved photoemission can be used to spectroscopically detect transient topological states in graphene. Phys. Rev. X **10**, 041013 (2020).

60. Dabiri, S. S. & Asgari, R. Time-dependent Berry curvature and quantum metric of Floquet-Bloch states. arXiv:2608.01096 (2026).

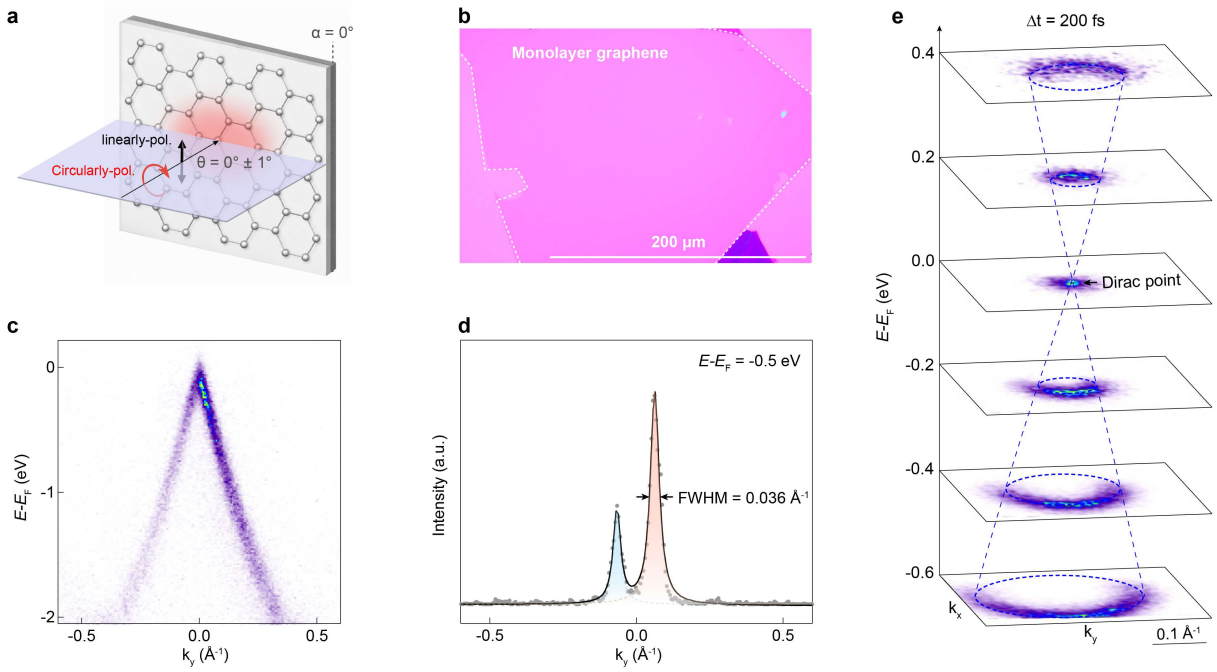
61. Perez-Piskunow, P. M., Foa Torres, L. E. F. & Usaj, G. Hierarchy of Floquet gaps and edge states for driven honeycomb lattices. Phys. Rev. A **91**, 043625 (2015).

Data availability All data supporting the results of this study are available within the article. Additional data are available from the corresponding author upon request.

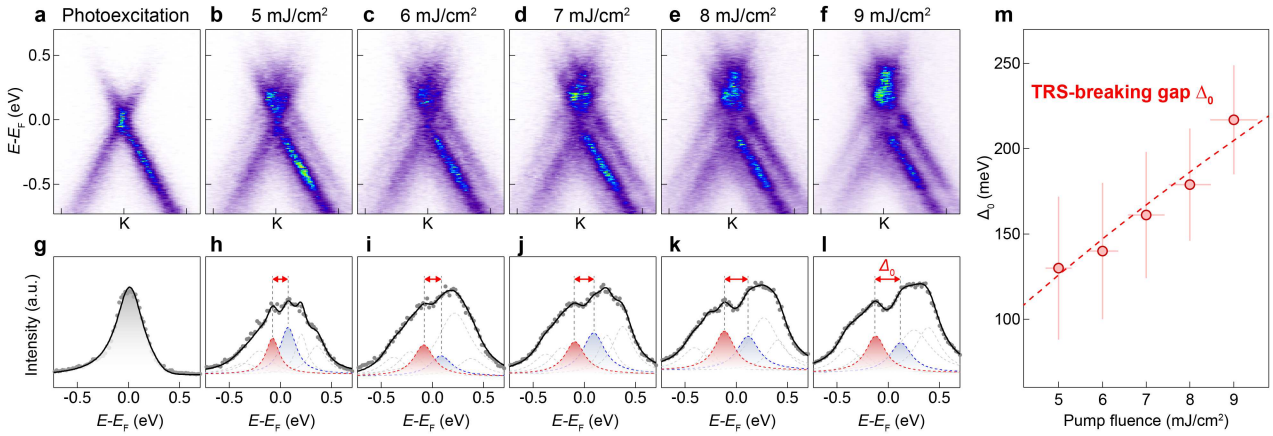
Acknowledgement This work is supported by the National Natural Science Foundation of China (grant numbers 12421004 and 12234011), Tsinghua University Initiative Scientific Research Program (grant number 20251080106), National Key R&D Program of China (grant number 2021YFA1400100), the National Natural Science Foundation of China (grant numbers 12327805, 52388201 and 12374291) and New Cornerstone Science Foundation through the XPLORER PRIZE. A.R. acknowledges support by the European Research Council (ERC-2024-SyG-101167294; UnMySt), the Cluster of Excellence Advanced Imaging of Matter (AIM), Grupos Consolidados Gobierno Vasco (IT1453-22), and the support from the Max Planck-New York City Center for Non-Equilibrium Quantum Phenomena. The Flatiron Institute is a division of the Simons Foundation. P.T. was supported by the National Key Basic Research and Development Program of China (Grants No. 2024YFA1409100), the National Natural Science Foundation of China (Grants No. 12234011 and No. 12374053), and the Suzhou National Laboratory (SK-1902-2026-004).

Author Contributions S.Z. conceived the research project. F.W. and X.C. performed TrARPES measurements and analyzed the data. W.C., Jinxi L. and Jiansong L. prepared the samples. X.C. contributed to the development and optimization of the HHG light source. Jinze L. and Z.S. performed the theoretical calculations. B.F., P.T., W.D., A.R. and P.Y. discussed the results. F.W., Jinze L., P.Y., Z.S., and S.Z. wrote the manuscript, and all authors commented on the manuscript.

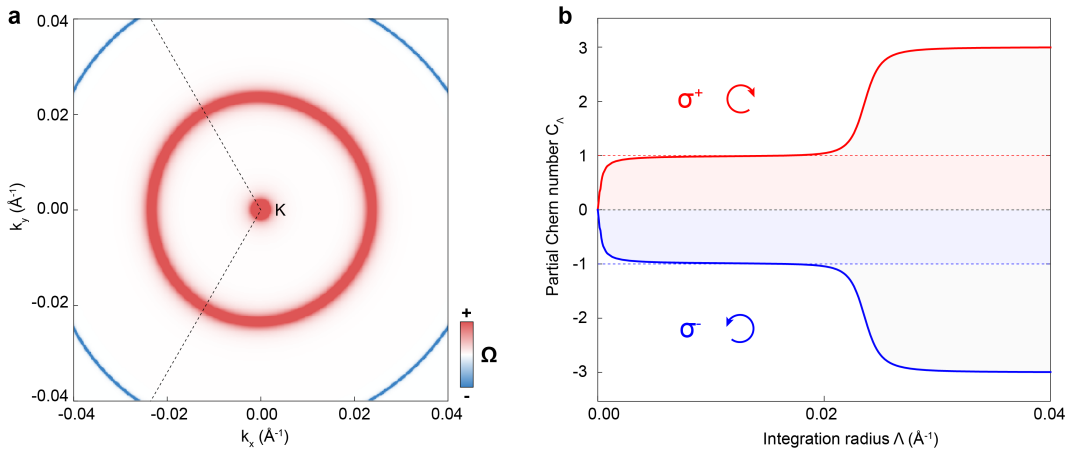
Competing Interests The authors declare that they have no competing financial interests.



Extended Data Fig. 1 | Characterization of the monolayer graphene sample. **a**, Schematic of the sample structure and the experimental geometry. The pump is incident on the monolayer graphene sample at near normal angle. **b**, Optical image of monolayer graphene sample used in this study. **c**, Equilibrium ARPES dispersion of monolayer graphene. **d**, Momentum-distribution curve (MDC) extracted at $E - E_{\mathrm{F}} = -0.5$ eV from the ARPES dispersion in **c**. The sharp MDC peak reflects the high-quality of the MLG sample. **e**, TrARPES dispersion measured at $\Delta t = 200$ fs with a pump photon energy of 310 meV and a pump fluence of 9.0 mJ/cm^2.



Extended Data Fig. 2 | Pump fluence dependence of the Floquet-induced Dirac gap. **a**, TrARPES dispersion image measured at $\Delta t = 200$ fs. **b-f**, TrARPES dispersion images measured $\Delta t = 0$ under circularly polarized driving at different pump fluence. **g-l**, Corresponding EDCs extracted from (**a-f**) at the K point with fitting curves appended. **m**, Extracted Floquet-induced Dirac gap as a function of the pump fluence.



Extended Data Fig. 3 | Light-induced Berry curvature and Floquet Chern topology. a, Calculated momentum-resolved Floquet Berry curvature of the lower Floquet band around the K valley. **b**, The partial Chern numbers C_Λ (including both valleys) as functions of the momentum cutoff Λ for RCP (σ^+) and LCP (σ^-) with a weak pump field, respectively.